Dynamics of an Actively Controlled Plain Trailing Edge Flap System for a Modern Bearingless Rotor

Judah Milgram* Inderjit Chopra †

Alfred Gessow Rotorcraft Center
Department of Aerospace Engineering
University of Maryland
College Park, Maryland 20742

A comprehensive analysis developed to evaluate plain trailing edge flap systems for vibration reduction is used to conduct a parametric study for a five-bladed bearingless rotor. The analytic model includes a bearingless rotor formulation, an advanced compressible, unsteady aerodynamic model, a free wake analysis, and a multicyclic algorithm for determining flap inputs. A correlation study for the basic rotor was performed using test data from a typical 5-bladed bearingless rotor system. The results were mixed, with good correlation in inplane oscillatory bending loads but poor agreement in flatwise bending and hub loads. These difficulties are attributed to test stand dynamics, which are not included in the analysis. The parametric study predicted reductions in the vibration objective function of over 90%, using plain trailing edge flap motions. Spanwise placement of the trailing edge flap appears to be a critical parameter in determining power actuation requirements, but has less of an effect on the flap's ability to reduce vibration. Small variations in blade bending and torsional stiffness had little effect on the overall flap system performance.

Nomenclature

C_T	Coefficient of thrust, $T/\rho\Omega^2 R^2 \pi R^2$
EI_y, GJ	Blade flatwise bending and torsional stiffness (normalized to $\Omega^2 R^2 m_{\text{ref}}$)
F_x, F_y, F_z	Fixed system hub longitudinal, lateral, and vertical shear. Normalized to $\Omega^2 R^2 m_{\text{ref}}$
J	Scalar nondimensional vibration objective function
M_h	Trailing edge flap hinge moment, positive moment increases δ. Normalized to $\Omega^2 R^3 m_{\text{ref}}$
M_x, M_y	Fixed system hub rolling and pitching moments. Normalized to $\Omega^2 R^3 m_{\text{ref}}$.
$M_\beta, M_\zeta, M_\theta$	Blade sectional moments: flatwise bending, inplane bending, and torsion (normalized to $\Omega^2 R^3 m_{\text{ref}}$).
N_b	Number of blades
P_f	Flap actuator power required, normalized to $\Omega^3 R^3 m_{\text{ref}}$
R	Rotor radius (dimensional)
a	Nominal profile lift curve slope
c	Nominal blade chord; also, chord of two dimensional flap/airfoil section (dimensional)
c_f	Flap chord (dimensional)
c_l	Profile lift coefficient
c_m	Profile pitching moment coefficient
l_f	Flap length, normalized to R
m_{ref}	Reference blade mass per unit span, $3c\rho_0 aR/\gamma$ (dimensional)
r_{mid}	Spanwise location of flap midpoint (dimensional)
s	Scaling factor applied to flap controller output
α	Shear/Moment weighting parameter in multicyclic algorithm
β	Flap input weighting parameter in multicyclic algorithm
α_s	Rotor shaft angle, positive for shaft tilting nose down
γ	Lock number, $c\rho_0 aR^4/I_\beta$

*Research Associate
†Professor and Director

Presented at the 23rd European Rotorcraft Forum, Dresden, Germany, September 16-18, 1997

δ	Flap deflection, positive for flap deflecting trailing edge down
$\delta_{\max}$	Maximum permissible value of $\|\delta\|$
$\varepsilon_N, \varepsilon_M, \varepsilon_H$	Empirical aerodynamic efficiency factors for incremental lift, moment, and hinge moment
η_p	Flap actuator power recovery factor
μ	Advance ratio, $V/\Omega R$
ρ, ρ_0	Actual and nominal ambient density
σ	Rotor solidity, $N_b c/\pi R$
ψ	Blade azimuth angle
θ_{tw}	Nominal blade twist
ω_n	Frequency of blade normal mode (dimensional)
Ω, Ω_0	Actual and nominal rotor speed (dimensional)
$\mathbf{C}, \mathbf{C}_{\boldsymbol{\theta}}, \mathbf{D}$	Matrices for computing control updates
$\mathbf{I}$	Identity matrix
$\mathbf{T}$	Sensitivity matrix in multicylic algorithm
$\mathbf{W}_z$	Weighting matrix for fixed system hub loads
$\mathbf{W}_\theta$	Weighting matrix for control input harmonics
$\mathbf{W}_{\Delta\theta}$	Weighting matrix for time derivatives of control input harmonics
$\mathbf{z}$	Vector of harmonic coefficients of fixed system hub loads
$\boldsymbol{\theta}$	Vector of coefficients of flap inputs (degrees)
$\Delta\boldsymbol{\theta}$	$\boldsymbol{\theta}_n - \boldsymbol{\theta}_{n-1}$ (degrees)
$\overset{*}{(..)}$	$d/d\psi$
$(..)_n$	At nth time step
$(..)_0$	Uncontrolled

Introduction

Early in the course of rotorcraft development, the feathering blade controlled by a swashplate emerged as the favored form of rotor control. The swashplate provides a mechanically simple means of providing a 1/rev feathering input to the blades; this is precisely what is required to meet the basic need to control the rotor thrust vector. Nevertheless, it may be noted that the earliest successful implementation of 1/rev cyclic control utilized a trailing edge flap [1].

Subsequently, the recognition that fixed system vibration arises primarily as a result of the aerodynamic environment at the rotor disk and blade motion at higher rotor harmonics led naturally to the concept of higher harmonic (mutlicyclic) control. Here too it may be observed that one of the earliest studies in multicyclic control identified the servo flap as a means for the implementation of higher harmonic blade control inputs [2]. Multicyclic control may be implemented through swashplate inputs or via individual actuators in the rotating system (Individual Blade Control, IBC). Vibration reduction systems utilizing trailing edge flaps have been the subject of several experimental and analytical studies in recent years. In addition to the advantages offered by Individual Blade Control (IBC) systems, trailing edge flaps offer the possibility for actuation through induced strain smart actuators. Such actuators are mechanically simple, eliminating the need for a hydraulic slipring, and have the high bandwidth required for use with multicyclic and/or time domain control systems. Induced strain actuation systems for trailing edge flaps have been investigated recently by several researchers, including Spangler and Hall [3], Walz and Chopra [4], Bernhard and Chopra [5], and Koratkar and Chopra [6], Straub [7] and Fulton and Ormiston [8].

An early analytic and experimental study of multicyclic control using servo-flaps conducted by Lemnios and others [9, 10] predicted appreciable reductions in vibration of a four-bladed rotor with single frequency 2/rev flap inputs. Subsequently, Millott and Friedmann [11, 12] used a more detailed analysis to investigate servo-flaps for a typical hingeless rotor configuration. Their investigation used a modified quasisteady version of Greenberg's aerodynamic theory. The flap was assumed to be driven at a number of discrete harmonics determined by a discrete time controller updating no more than once per revolution. This is essentially a servo flap implementation of a conventional HHC scheme (see, for example, Ref. 13). The updates were made based on harmonic content of the rotating system hub loads. The study included parametric studies of flap size, flap location, and blade torsional stiffness. The servo flap system was found to be just as effective as conventional (blade-root actuation) multicyclic control, with greatly reduced power requirements. The flap location was determined to be a significant design parameter, with the flap most effective when centered near the node of the blade second flatwise bending mode.

Despite their apparent promise and successful service history in 1/rev cyclic control applications, servo flaps present some difficulties such as increased rotor profile power due to the exposure of the hinge and support structures to the free stream, reduced aerodynamic efficiency due to the flap hinge gap, and potential maintainability problems. An alternative configuration, the plain trailing edge flap, is the subject of the present investigation. Here the flap is integrated into the rotor blade in the manner of the aileron of a fixed-wing aircraft (indeed, plain flaps were termed "ailerons" by Sikorsky [14]). By locating the flap support structure, hinge, and linkage assembly internally within the blade profile, its aerodynamic drag and susceptibility to damage may be greatly reduced. In addition, the hinge gap may be completely sealed.

Plain trailing edge flaps have been investigated previously by Dinkler and Doengi [15], Straub *et al.* [7, 16–18], as well as by the authors [19–21]. Reference 15 documents an analytic study with emphasis on various robust control algorithms; the physical model itself incorporates several key simplifications such as quasisteady aerodynamics and uniform inflow. Issues such as flap sizing and placement are not discussed. References 16 and 18 discuss wind tunnel tests of a 12 foot diameter model rotor with plain flap. In earlier studies by the authors [19–21], a comprehensive aeroelastic analysis with unsteady aerodynamics and free wake model was developed to evaluate the potential for vibration reduction with trailing edge flaps. Reference 19 contains a preliminary open loop study. In Refs. 20 and 21, an extensive correlation study was conducted using experimental data from a wind tunnel model test of an active flap system. Reference 21 presents a detailed parametric design study for a trailing edge flap system for an existing articulated rotor. The results indicated that significant reductions in fixed system vibration are possible with a properly sized and located flap.

In Ref. 21, the flap system was evaluated as a retrofit system to an existing rotor; the structural dynamic properties of the blade itself remained unchanged. However, smart materials actuated trailing edge flap systems are perhaps more likely to find application in advanced rotor systems. In this case, it becomes important to integrate the rotor and flap system designs for optimum effect.

The goal of the present investigation is to examine the potential for the integrated design of an actively controlled plain trailing edge flap system with a modern bearingless rotor. For this study, the characteristics of a typical bearingless rotor are taken as a starting point.

Analytic model

The present analysis is based on UMARC (University of Maryland Advanced Rotorcraft Code). The basic analysis and recent extensions to allow modeling of the trailing edge flap are discussed in References 19–22. The following briefly outlines the analysis and solution procedure.

The blade is discretized into a number of one-dimensional beam elements, each with 15 degrees of freedom. Sixteen spatial elements are used to model the rotor blade used in the present study. The aeroelastic equations of motion are solved using modal reduction, in this case using seven normal modes, including the first four flatwise modes, the first two inplane modes, and the first torsional mode (the fourth flatwise mode exhibits significant torsional motion as well). The periodic equations of motion are solved using the finite element in time method with six equally sized time elements and sixth order polynomials as time basis functions. Mixed Lagrange-Hermite polynomials are used to enforce continuity of velocity between time elements.

The spatial elements may be modeled with a trailing edge flap, allowing for an array of independently moving flaps along the blade. In the present study the flap motions are prescribed. Flap inertial effects are included both in the formulation of the blade equations of motion and the hub loads computation.

A bearingless rotor model was employed, featuring multiple load paths for flexbeam/torque tube configuration, viscoelastic snubber, kinematics of control linkage, and nonlinear bending-torsion coupling within the flexbeam [23].

The analysis uses the time-domain unsteady aerodynamic model of Hariharan and Leishman [24]. This advanced model features an indicial approach for both circulatory and non-circulatory unsteady loads due to airfoil and flap motion. Compressibility effects in the non-circulatory airloads are properly captured. The flap hinge gap is assumed to be completely sealed, although viscous effects on the flap efficiency may be represented using empirical efficiency factors ε_N, ε_M, and ε_H, that are applied to the incremental profile lift, pitching moment, and hinge moment resulting from flap motion. All results presented here are based on the free wake model developed by Bagai and Leishman [25]. The rotor is trimmed to zero first harmonic flapping and a constant C_T/σ. The shaft angle is adjusted to provide propulsive trim. The hub and blade sectional loads are calculated by integration of the inertial and aerodynamic forces acting on the blade.

An initial study using open-loop, single frequency flap inputs (Refs. 19, 21) indicated that significant reductions in individual components of the N_b/rev hub loads are possible, requiring relatively little flap input. However, the penalty for off-optimum single-frequency inputs was shown to be quite high, and it was generally impossible to identify a single-frequency input that provides significant reductions in all hub load components. Although such open loop studies are useful for developing insight into the sensitivity of the rotor system to different combinations of trailing edge flap multicyclic input, they are impractical for use in a parametric design study due to the need to investigate a large number of flap inputs for each configuration. Hence, a multicyclic control algorithm is used to determine the flap inputs for each configuration. The algorithm used in this study is described in Ref. 13. A scalar vibration objective function J is defined as

$$J \equiv \mathbf{z}_n^T \mathbf{W}_z \mathbf{z}_n + \boldsymbol{\theta}_n^T \mathbf{W}_\theta \boldsymbol{\theta}_n + \Delta\boldsymbol{\theta}_n^T \mathbf{W}_{\Delta\theta} \Delta\boldsymbol{\theta}_n \qquad (1)$$

Here $\mathbf{z}_n$ is a hub loads vector containing the cosine and sine coefficients of the N_b/rev fixed system hub loads F_x, F_y, F_z, M_x, and M_y at time step n. $\boldsymbol{\theta}_n$ and $\Delta\boldsymbol{\theta}_n$ represent the harmonics of the control inputs and control rates, respectively. The diagonal matrices $\mathbf{W}$ contain weights for different harmonics of the vibration ($\mathbf{W}_z$), the control inputs ($\mathbf{W}_\theta$) and the control rates ($\mathbf{W}_{\Delta\theta}$). The controller may be based on either a global linearization assumption

$$\mathbf{z}_n = \mathbf{z}_0 + \mathbf{T}\boldsymbol{\theta}_n \qquad (2)$$

or a local linearization assumption

$$\mathbf{z}_n = \mathbf{z}_{n-1} + \mathbf{T}(\boldsymbol{\theta}_n - \boldsymbol{\theta}_{n-1}). \qquad (3)$$

In Equations 2 and 3, $\mathbf{z}_0$ is the uncontrolled vibration vector. The sensitivity matrix $\mathbf{T}$ relates the linearized system response to multicyclic control inputs.

Equation 3 applies to both the global and local linearizations. Substituting Equation 3 into Equation 1 and minimizing J by solving $\partial J / \partial \theta_{n_i} = 0$ for each of the elements i in the control vector $\boldsymbol{\theta}_n$ yields the local model algorithm for updating the control inputs $\boldsymbol{\theta}_n$ [13]:

$$\Delta\boldsymbol{\theta}_n = \mathbf{C}\mathbf{z}_{n-1} - \mathbf{C}_{\boldsymbol{\theta}}\boldsymbol{\theta}_{n-1} \qquad (4)$$

This may be simplified using Equation 2, leading to the global controller:

$$\Delta\boldsymbol{\theta}_n = \mathbf{C}\mathbf{z}_0 - (\mathbf{C}_{\boldsymbol{\theta}} - \mathbf{C}\mathbf{T})\boldsymbol{\theta}_{n-1} \qquad (5)$$

In Equations 4 and 5 the following definitions apply:

$$\begin{aligned} \mathbf{C} &= -\mathbf{D}\mathbf{T}^T\mathbf{W}_z && (6) \\ \mathbf{C}_{\boldsymbol{\theta}} &= \mathbf{D}\mathbf{W}_\theta && (7) \\ \mathbf{D} &= \left(\mathbf{T}^T\mathbf{W}_z\mathbf{T} + \mathbf{W}_\theta + \mathbf{W}_{\Delta\theta}\right)^{-1} && (8) \end{aligned}$$

Current smart structure actuators are limited in their output stroke. This is modeled by scaling the vector of flap harmonics as directed by the controller by a factor s, defined as

$$s = \min\left(\frac{\delta_{\max}}{||\delta(\psi)||_\infty}, 1\right) \qquad (9)$$

In the present study, a value of $\delta_{\max} = 10°$ was chosen, whereby it is noted this value exceeds the capability of present day actuators.

In both the local and global controllers, the sensitivity matrix $\mathbf{T}$ is computed once at the uncontrolled operating condition using a forward difference method. In general, it is expected that global controller will provide the best stability since it incorporates no feedback of the response. On the other hand, performance may be poor if significant nonlinearities exist or if the operating condition differs significantly from that at which the sensitivity matrix T was determined. Some researchers have considered more advanced controllers, in which the estimated $\mathbf{T}$ is updated along with the control inputs. However, the fixed-gain approach used in the present investigation has been successfully demonstrated in a wind tunnel test [26].

In the present research, the weighting matrix $\mathbf{W}_z$ is assumed to have the form

$$\mathbf{W}_z = (1-\beta)\begin{bmatrix} \alpha & & & & \\ & \alpha & & & \\ & & \alpha & & \\ & & & 1-\alpha & \\ & & & & 1-\alpha \end{bmatrix} \qquad (10)$$

The first three elements are the weights for the hub shears, and the final two weights are the weights for the hub moments. By allowing the nondimensional parameter α to vary from zero to unity, the controller may be instructed to give more importance to reducing either hub moments or hub shears. A nominal value of $\alpha = 0.5$ signifies that all normalized hub forces and moments are to be weighted equally. The nondimensional parameter β in Equation 10 is used in conjunction with the flap motion weighting matrix $\mathbf{W}_\theta$ to establish the relative importance of hub loads versus flap inputs in the objective function J. $\mathbf{W}_\theta$ is assumed to be of the form

$$\mathbf{W}_\theta = \beta\,\mathbf{I} \qquad (11)$$

With $\beta = 0$, the controller will attempt to minimize hub loads without regard to the trailing edge flap motions or flap power requirements. As β increases from $\beta = 0$, the controller will gradually reduce trailing edge flap motions to zero, allowing the vibratory hub loads to remain at their uncontrolled level. The present investigation considers only steady state trimmed operating conditions, and the control rate weighting matrix $\mathbf{W}_{\Delta\theta}$ is assumed zero.

The mean power required by the flap actuator is obtained by integrating the product of the hinge moment and flap deflection over the azimuth:

$$P_f = -\frac{N_b}{2\pi}\int_0^{2\pi} M_h\,\overset{\star}{\delta}\;d\psi \qquad (12)$$

The flap power required may change sign over some portions of the azimuth, and as the actuator will generally not be able to transfer power back to its power

Table 1: Summary of MD-900 basic design data and reference parameters

Number of blades	N_b	5
Rotor radius	R	16.925 ft
Rotor speed	Ω_0	392 RPM (41.1 1/s) (nominal)
Chord	c/R	0.0492 (nominal)
Reference profile lift curve slope	a	2π
Ambient density	ρ_0	0.002378 slug/ft^3
Lock number	γ	9.17 (nominal)
Solidity	$N_b c/\pi R$	0.0779
Twist	θ_{tw}	10° (nominal; actual value by table lookup)
Reference mass/span	m_{ref}	0.0655 slug/ft
Reference linear damping	$m_{ref}\Omega_0 R$	45.5 lb-s/ft
Reference linear stiffness	$m_{ref}\Omega_0^2 R$	1,870 lb/ft
Reference shear	$m_{ref}\Omega_0^2 R^2$	31,600 lb.
Reference moment	$m_{ref}\Omega_0^2 R^3$	535,000 ft-lb
Reference bending and torsional stiffness	$m_{ref}\Omega_0^2 R^4$	$9.06 \cdot 10^6$ lb-ft^2

supply with full efficiency, a power recovery factor $f(M_h, \delta)$ is applied to the instantaneous flap power required $M_h \overset{\star}{\delta}$ in Equation 12 as follows:

$$f = \begin{cases} 1 & \text{for } M_h \overset{\star}{\delta} \leq 0 \\ \eta_p & \text{for } M_h \overset{\star}{\delta} > 0 \end{cases} \tag{13}$$

The present study assumes a value of $\eta_p = 0$.

Correlation Study

Active Flap Rotor

The predictive capabilities of the flap analysis were evaluated in [20,21] by comparing analytic results with wind tunnel test data for the McDonnell-Douglas Active Flap Rotor (AFR) [17]. The AFR was a four-bladed fully articulated model of 12 ft. diameter featuring plain trailing edge flaps of $c_f/c = 0.25$ extending from .79-.97R. The flaps were driven via a cam and pulley arrangement. The experimental data reflect both flap-fixed and active flap cases. The analysis used in the Ref. 21 study utilized an earlier version of the free wake analysis (Scully-Johnson model). This correlation study showed fair correlation between predicted and measured trim controls in forward flight, with the exception of lateral cyclic. Good agreement was seen in the rotor power required. For the baseline rotor (zero flap motion), the overall agreement in the measured blade loads was fair. Discrepancies were observed in the low speed ($\mu = 0.10$) 1/rev in-plane bending moment; this discrepancy appeared to be related to the inflow modeling. In some cases, considerable differences in the steady values of the blade loads were observed; these were attributed to simplifications in the analytic model (in particular, a flap bellcrank extending above the upper surface of the blade was not modeled). With flap motion at 5/rev, the overall correlation was fair. Good agreement was seen in the torsional moments, while certain flatwise bending parameters showed significant discrepancies. The analysis showed mixed success at predicting the effects of varying the phase angle of the trailing edge flap input. In many cases, the unsteady aerodynamic

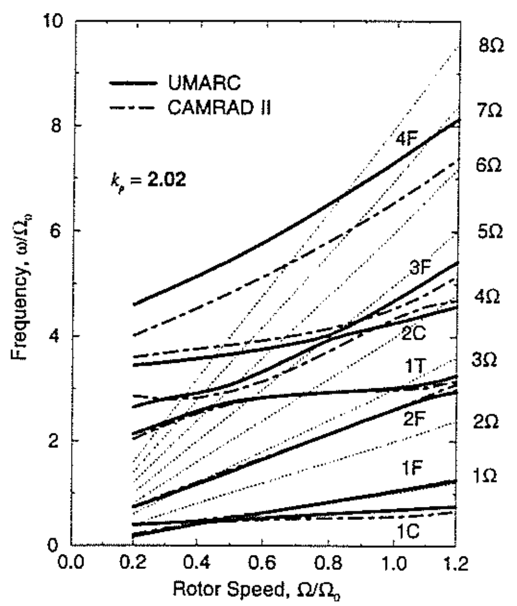

Figure 1: Comparison of blade normal mode frequency predictions for MD-900 bearingless main rotor

Table 2: Calculated normal mode frequencies for MDART rotor on wind tunnel test stand at $\Omega = \Omega_0$

Mode	Frequency (per rev)
1st inplane	0.69
1st flap	1.057
2nd flap	2.68
2nd inplane	4.28
3rd flap	4.69
1st torsion	6.29
4th flap	7.68

Table 3: Operating conditions for correlation study

Advance Ratio μ (deg.)	Shaft Angle α_s (deg.)	Thrust C_T/σ
.151	-2.6	.07560
.200	-4.9	.07372
.248	-6.9	.07514
.299	-3.8	.07771
.349	-10.9	.07515
.373	-11.8	.07455

model improved the phase correlation.

Bearingless Rotor

The analysis used in the present investigation incorporated an advanced Bearingless Main Rotor (BMR) model and an additional correlation study was performed utilizing experimental data from the McDonnell-Douglas Advanced Rotor Technology (MDART) program conducted at NASA-Ames in the early 1990's [27–29]. The bearingless MDART rotor was a preproduction version of the MD-900 Explorer. A full scale rotor of 34 foot diameter was tested. Table 1 summarizes the basic design data for the MDART rotor. The detailed design data used in the present study were based on the analytic model of Reference 29, together with information provided by the manufacturer.

Figure 1 compares computed normal modes from the present analysis with results obtained by McDonnell-Douglas using CAMRAD II. The UMARC model predicts a slightly higher blade first inplane natural frequency than that predicted by CAMRAD. This may be a result of different values of snubber stiffness used in the analyses (the present analysis assumes a value consistent with Reference 29, while the CAMRAD results in Figure 1 are based on a lower value). Good agreement is seen for the first and second flatwise bending modes, the second chordwise mode, and the first torsion mode. A significant discrepancy exists in the fourth flatwise bending mode predictions. This mode actually involves significant torsional deflection, and a higher order coupled mode of this nature would be expected to be sensitive to modeling assumptions. Note that these results were computed based on a pushrod stiffness applicable to the flight vehicle, while the remainder of the correlation study assumes a considerably higher value as applicable to the wind tunnel test stand. Normal mode frequencies for this wind tunnel case are summarized in Table 2 for $\Omega = \Omega_0$.

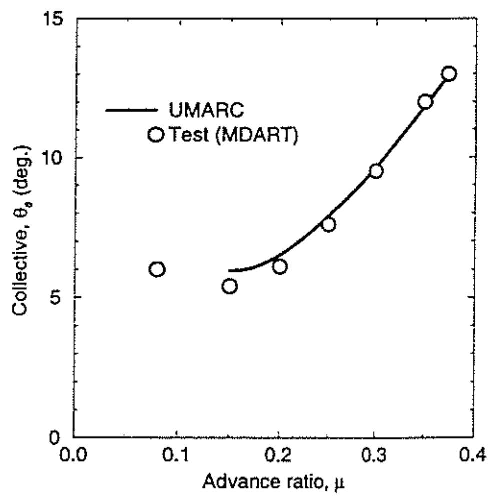

Figure 2: Measured and predicted collective pitch (θ_{75}) vs. advance ratio, μ

The rotor was tested in hover and forward flight up to $\mu = 0.373$. Table 3 summarizes the operating conditions for different forward flight cases. The rotor was trimmed to zero first harmonic flapping and to the thrust shown in Table 3. For this correlation study, rather than using the collective control positions used in the wind tunnel test, the analytic model was trimmed to the measured values of C_T/σ listed in Table 3.

Figures 2 and 3 compare the measured and predicted trim controls. Figure 2 shows good agreement between the measured and calculated collective pitch. Figure 3 shows both longitudinal and lateral cyclic control positions as a function of advance ratio. The longitudinal cyclic (θ_{1S}) shows good agreement at the low advance ratios, although the discrepancy grows with increasing speed up to approximately 1°at $\mu = .373$. The lateral cyclic shows fair agreement at low advance ratio, however, the analysis predicts a different trend with increasing advance ratio, leading to

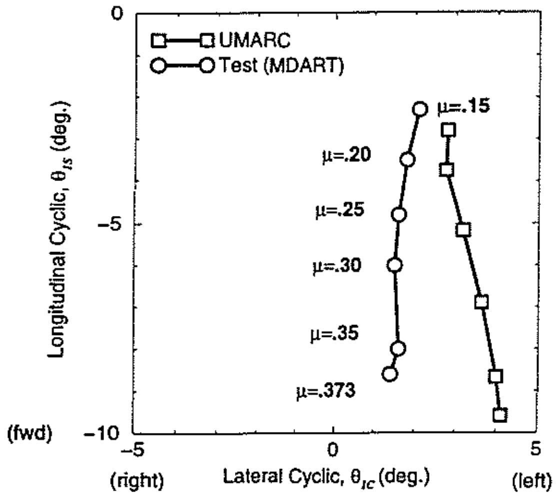

Figure 3: Measured and predicted cyclic control vs. advance ratio, μ

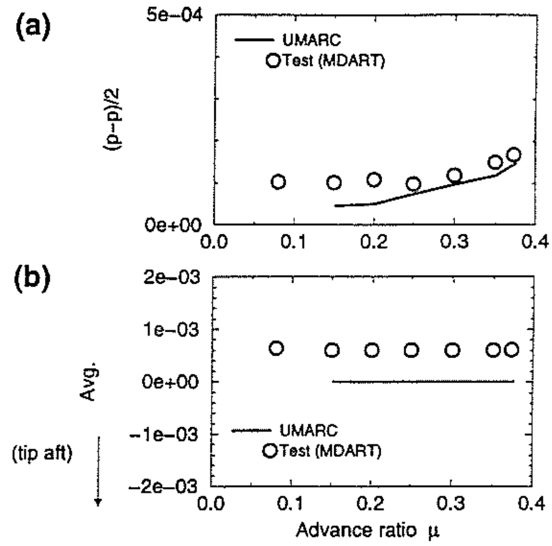

Figure 4: Measured and predicted blade inplane bending (M_ζ) at station .807R vs. advance ratio, μ. (a) Cyclic (peak-peak/2) (b) Average

a 2.5°difference at $\mu = 0.373$. Lateral cyclic is, in general, sensitive to inflow modeling and blade flapping dynamics.

Table 4: MDART measurements for correlation study

Location	Measurement
Blade, .34R	M_β, M_ζ, M_θ
.43R	M_β
.81R	M_β, M_ζ
.89R	M_β
Hub	F_x, F_y, F_z, M_x, M_y

Figures 4-10 present blade sectional loads in the rotating system. The measurements used for comparison are listed in Table 4. The data are presented as average and cyclic (peak-peak/2) components versus advance ratio. Figures 4 and 5 compare the inplane bending moment (M_ζ) at .807R and .344R, respectively. The overall inplane bending moment correlation is fair. At .807R (Fig. 4), the advance ratio trend is well captured and the agreement is better at the higher advance ratios. The agreement in the average component is also good; the flat trend with advance ratio is properly predicted with only a constant offset from the measured values. Again at .344R (Fig. 5), the predicted cyclic components agree well with the measured values. The predicted average value at this location agrees fairly well. The trend is captured very well with only a relatively small offset from the measured data.

Somewhat less success was achieved in predicting the flatwise bending moments. Figures 6-9 show the blade flatwise bending (M_β) at four spanwise stations. At the outboard station (.891R, Fig. 6), the agreement is fair, with good correlation in steady value. However, the trend in vibratory component is not well represented, with the analysis predicting a steady increase in peak-to-peak values with increasing advance ratio. The test data, on the other hand, show surprisingly little variation with airspeed. At the other inboard stations, (.807R, .428R, and .344R) the agreement is poor (Figures 7-9), both in magnitude of the peak-peak values as well as their trends. The steady bending moments also show considerable differences.

An examination of the analytically predicted waveform shows that the large monotonic increase in peak-peak values with advance ratios due primarily to a large increase in 3/rev flatwise bending. These two inboard stations are in fact located in a region where the bending due to motion in the second flatwise bending mode is at a maximum. This bending mode has a frequency near 3/rev and apparently is readily excited by 3/rev airloads in forward flight. These discrepancies in flatwise bending continue to be a focus of the present research. The earlier correlation study (Refs. 20 and 21) with the articulated rotor yielded considerably better results; the difficulty here may be traceable to test stand dynamics. A dynamic calibration of the wind tunnel test stand [29] identified significant test stand dynamic amplification factors for 5/rev shears and large couplings between the shears and moments resulting from the vertical offset between the balance center and hub. Hence, it is anticipated that, for this set of experimental data, good hub loads correlation

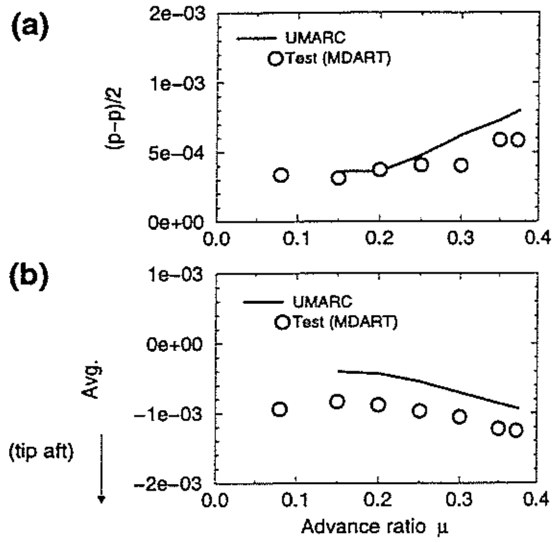

Figure 5: Measured and predicted blade inplane bending (M_ζ) at station .344R vs. advance ratio, μ. (a) Cyclic (peak-peak/2) (b) Average

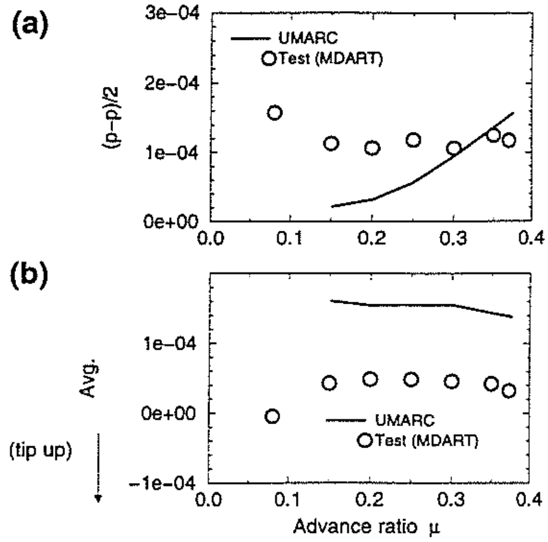

Figure 7: Measured and predicted blade flatwise bending (M_β) at station .807R vs. advance ratio, μ. (a) Cyclic (peak-peak/2) (b) Average

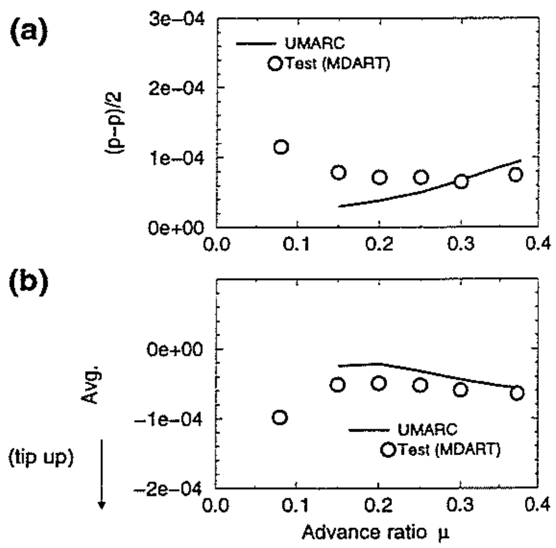

Figure 6: Measured and predicted blade flatwise bending (M_β) at station .891R vs. advance ratio, μ. (a) Cyclic (peak-peak/2) (b) Average

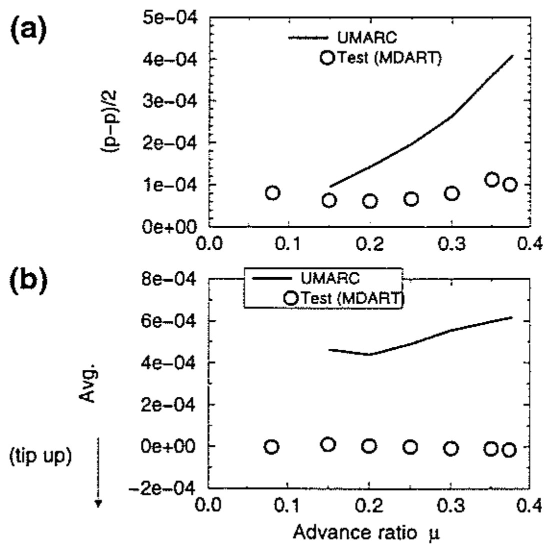

Figure 8: Measured and predicted blade flatwise bending (M_β) at station .428R vs. advance ratio, μ. (a) Cyclic (peak-peak/2) (b) Average

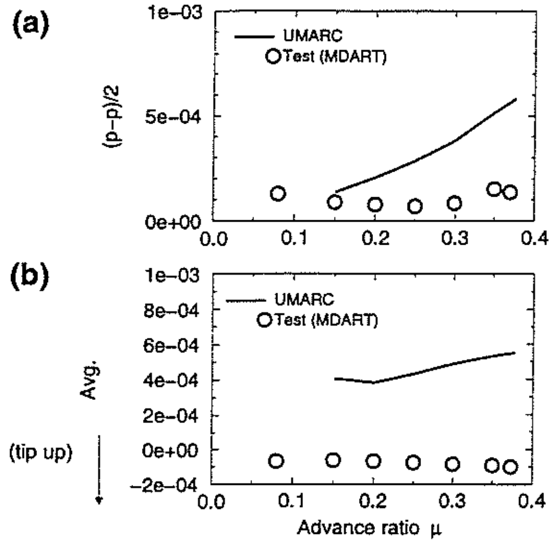

Figure 9: Measured and predicted blade flatwise bending (M_β) at station .344R vs. advance ratio, μ. (a) Cyclic (peak-peak/2) (b) Average

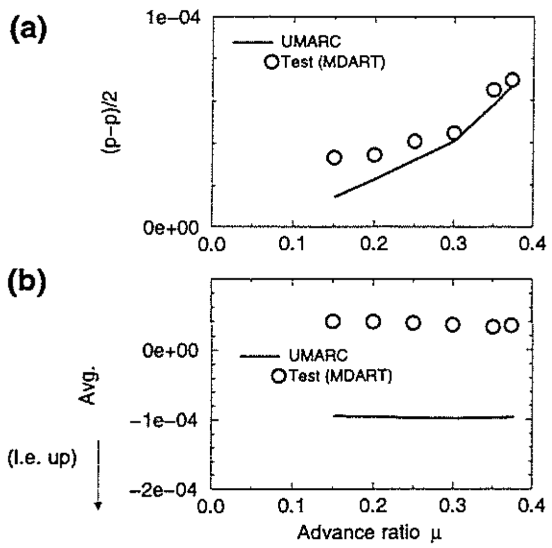

Figure 10: Measured and predicted blade torsional moment (M_θ) at station .344R vs. advance ratio, μ. (a) Cyclic (peak-peak/2) (b) Average

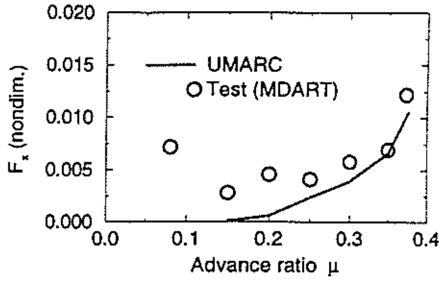

Figure 11: Measured and predicted 5/rev fixed system longitudinal hub shear (F_x) vs. advance ratio μ

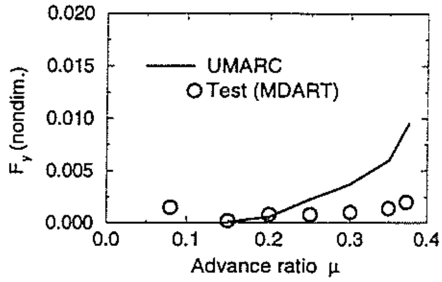

Figure 12: Measured and predicted 5/rev fixed system lateral hub shear (F_y) vs. advance ratio μ

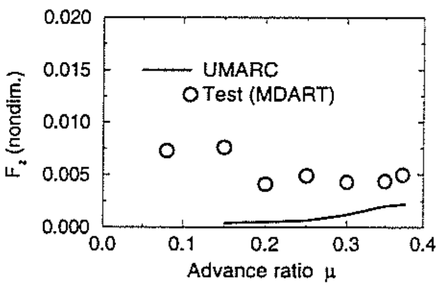

Figure 13: Measured and predicted 5/rev fixed system vertical hub shear (F_z) vs. advance ratio μ

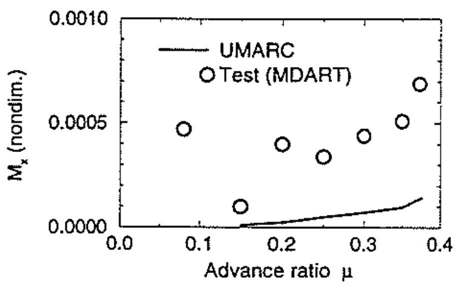

Figure 14: Measured and predicted 5/rev fixed system hub rolling moment (M_x) vs. advance ratio μ

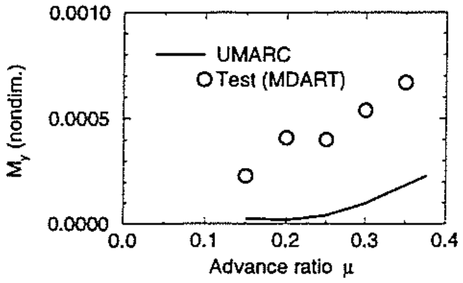

Figure 15: Measured and predicted 5/rev fixed system hub pitching moment (M_y) vs. advance ratio μ

will require implementation of a finite impedence hub model.

The predicted blade torsional moment at .344R (Fig. 10) shows very good agreement with the test results, both for steady and vibratory component.

Finally, Figures 11 to 15 present comparisons of the 5/rev fixed system hub loads. The agreement in longitudinal shear F_x (Fig. 11) is fairly good at the higher advance ratios, but degrades as the airspeed decreases. As was observed with the flatwise bending moment, the 5/rev lateral shear F_y (Fig. 12) displays the large increase with advance ratio that is not observed in the test data. The vertical 5/rev hub shear F_z (Fig. 13) and 5/rev hub moments M_x and M_y, (Figs. 14 and 15, respectively) show poor correlation with the measured test data.

Overall, the correlation study yielded mixed results. While the large differences between predicted and measured hub loads may be attributed to finite hub impedence of the wind tunnel test stand, the poor correlation in flatwise bending moment remains a concern. Although these discrepancies remain to be resolved, for the present study, which seeks to develop general conclusions concerning the combined effects of blade and flap design parameters, it is considered adequate.

Parametric Study

The goal of the present study is to examine the interaction of blade structural dynamic design with the design of the trailing edge flap system. The baseline rotor is the MDART bearingless main rotor used in the correlation study, simplified to reflect constant blade properties between the clevis ($0.30R$) and the beginning of the tapered tip ($0.93R$). The study was conducted for the rotor in wind tunnel trim at $\mu = 0.35$, $C_T/\sigma = .0746$, and $\alpha_s = 10°$ nose down. The trailing flap was assumed to have zero mass (the effects of variations in flap mass properties is discussed in

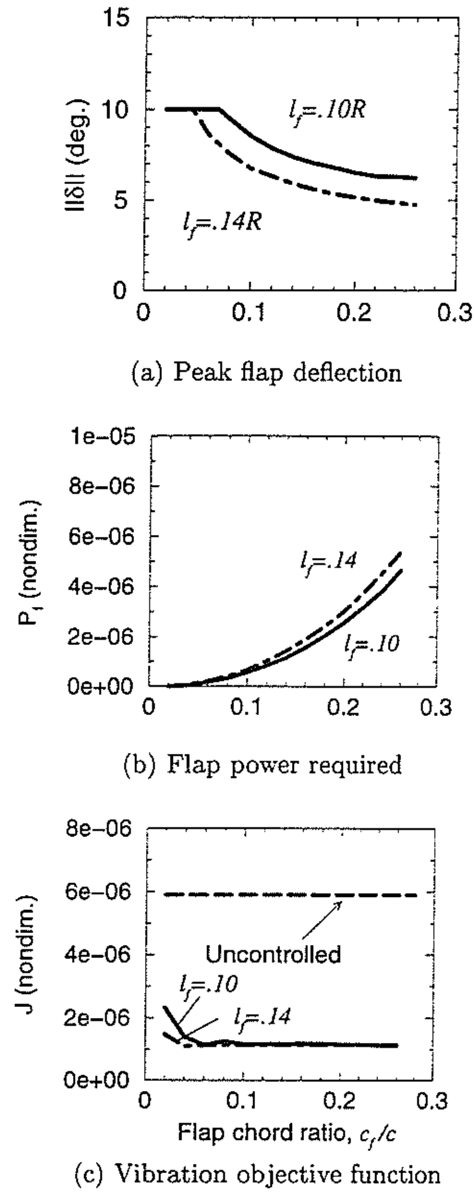

Figure 16: Effect of trailing edge flap-chord ratio (hinge location) on trailing edge flap system performance for two flap lengths, with r_{mid}=0.74, wind tunnel trim at $\mu = 0.35$, $\alpha = 5°$ nose down, and $C_T/\sigma = 0.080$ (S-76 studey, Ref. 21)

Reference 21). The control algorithm was applied to provide flap inputs at 4, 5, and 6/rev.

An earlier parametric design study by the authors [21] examined the influence of flap system design parameters such as flap length and depth, spanwise location, static imbalance, and controller weighting parameters. Several of these parameters were found to be relatively unimportant and are held at a fixed value in the present study. First, the flap length and depth were found to be of secondary importance because the controller automatically adjusts for changes in flap authority by varying the input amplitudes. Representative results are shown in Figure 16 for a four-bladed articulated rotor in wind tunnel trim at $\mu = 0.35$ [21]. The figure presents the controlled vibration objective function, the trailing edge flap power required, and the peak flap deflections as a function of flap chord ratio, c_f/c. The objective function results (Fig. 16(c)) show almost no change as the c_f/c is varied This reflects the multicyclic algorithm's ability to compensate for reductions in flap chord ratio by increasing the flap inputs. This increase in peak flap input as c_f/c is decreased is evident in Fig. 16(a). The flap deflections increase to the prescribed limit of 10° for small values of c_f/c. As may be expected, the flap deflections are larger and the limit is reached earlier for the smaller flap ($l_f = 0.10$). The trailing edge flap power required diminishes rapidly as the flap chord ratio is decreased. This is especially evident below $c_f/c = 0.06$, where the flap deflection limit is encountered. It is advantageous to keep the flap chord as small as possible without incurring excessive flap deflections. From approximately $c_f/c = 0.06$ to $c_f/c = 0.10$, both the $l_f = 0.10$ and $l_f = 0.14$ flaps produced nearly the same vibration reduction and required virtually the same actuation power.

In the present study, a flap chord ratio of $c_f/c = 0.20$ was selected to limit flap deflections and rates in order to ensure that nonlinear aerodynamic phenomena due to flow separation do not become a factor. The flap spanwise location was found to be an important parameter, and a relatively short flap of $l_f = 0.10R$ was selected to enhance the localized nature of the flap input. The flap is assumed to be mass-balanced about its hinge line. The controller weighting parameters are set to $\alpha = 0.10$ (favors reduction of hub shears over hub moments) and $\beta = 0$ (no consideration to minimizing flap deflections or flap power required). It was shown in Ref. 21 that the controller could compensate for reductions in flap aerodynamic effectiveness; in the present study no reduction in aerodynamic effectiveness is considered.

Baseline blade with bending stiffness variation

This section examines the performance of the actively controlled trailing edge flap system applied to the baseline bearingless rotor blade, along with the effects of variations in blade flatwise bending stiffness. For this study a relatively conservative bending stiffness variation of ±10% was considered.

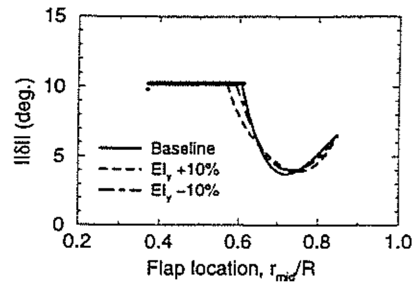

(a) Peak flap deflection

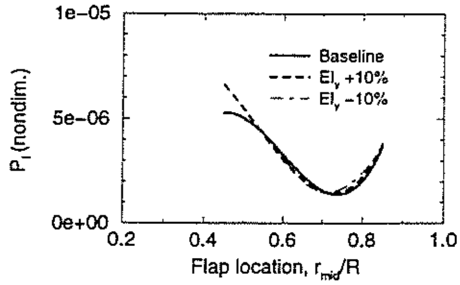

(b) Flap power required

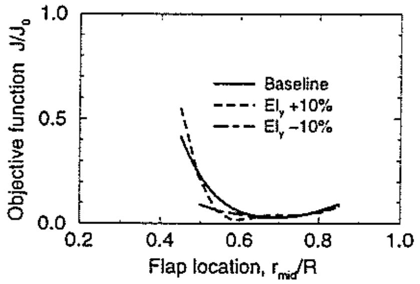

(c) Vibration objective function

Figure 17: Effect of trailing edge flap location (r_{mid}) on flap system performances for three values of blade flatwise bending stiffness, $EI_y$with wind tunnel trim at $\mu = 0.35$.

Figure 17 shows the trailing edge flap motion, power required, and resulting vibration objective function J as a function of the trailing edge flap spanwise location, r_{mid}. The flap is very effective at reducing vibration, with reductions in J greater than 90%. The strong influence of spanwise location is immediately apparent. For the vibration objective function (Fig. 17(c), shown normalized to its uncontrolled value) shows a shallow minimum with large reductions in vibration near r_{mid}=.70R. A large decrease in flap system performance occurs as the flap is moved inboard of approximately r_{mid}=.60R. With the 10% reduction in flatwise bending stiffness, this performance decrease is not as severe and flap locations as far inboard as r_{mid}=.50R appear feasible. Otherwise, no significant changes are observed with the flatwise bending stiffness variations shown. In Figure 17(b), a pronounced minimum in trailing edge flap power required is present around 0.70R. The power required at this location is less than half that required at r_{mid}=.60R. The bending stiffness variations have little influence, although at r_{mid}=.50R the flap requires more power when the blade bending stiffness is increased. The peak flap deflections are shown in Figure 17(a). Here again a pronounced minimum in flap deflection is seen around r_{mid}=.70R, consistent with the power requirements in Fig. 17(b). The flap input increases rapidly as the flap is moved inboard from this value, and the preset flap deflection limit of 10°is reached near r_{mid}=0.60. Near this flap location, the 10% increase in bending stiffness seems to lead to slightly reduced deflections.

The increased flap inputs and reduction in flap system performance as the flap is moved inboard from r_{mid}=.70R is attributed to the reduced dynamic pressure encountered at these locations. Nevertheless, it is interesting to note that the flap deflections also increase as the flap is moved outboard of r_{mid}=.70 (Fig. 17(a)), despite the increased dynamic pressure encountered near the blade tip. This shows that the effect of spanwise position is due not only to variations in dynamic pressure, but also to the blade structural dynamics. In Reference 21 (and Ref. 12, for the servo-flap case) the positioning effects are related to the modal deflections of the first several blade bending modes. Figure 18 shows the inplane and out of plane modal deflections for the second and third flatwise and second inplane modes. The analysis predicts a node for the second flatwise bending node at approximately .75R, near the location for best trailing edge flap performance. While it may be suggested that placing the flap near the node allows it to induce torsional motions in the blade without exciting this bending mode, the situation is somewhat more complex. This is apparent in Figure 19, which presents the time histories of the blade modal response for the uncontrolled and active flap controlled blade with r_{mid}=.75R. The flap indeed seems to influence primarily the torsional mode, inducing low amplitude higher harmonic components. However, the effects of the flap input is evident in the second and third flatwise modes as well, and it is not readily apparent whether this is due directly to the localized flap lift inputs, or whether it arises indirectly as a result of the torsional response.

It is interesting to note that as the flap is moved inboard of r_{mid}=.60R and the flap deflections reach their controller-limited value (Fig. 17(a)), the flap power requirements continue to increase (Fig. 17(a)) despite the flap deflections being limited to the established maximum of $||\delta|| = 10°$. Figure 20 compares the flap motions at r_{mid}=.45R and r_{mid}=.55R. At both locations the flap motions are subject to the controller limit. However, the .45R time history shows greater overall flap motions including a distinct higher frequency (6/rev) component that is not present with r_{mid}=.55R.

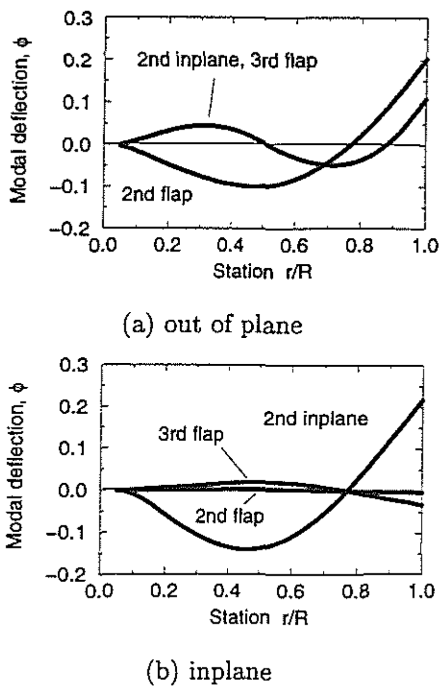

Figure 18: Mode shapes for baseline blade of 2nd flapping mode ($\omega_n/\Omega_0 = 2.6$), 2nd inplane mode ($\omega_n/\Omega_0 = 4.4$), and 3rd flapping mode ($\omega_n/\Omega_0 = 4.6$)

Influence of Torsional Stiffness

Figure 21 presents the flap system performance results for two values of blade torsional stiffness, representing variations from the baseline $GJ$of +10% and -10%. The results are similar to those for the baseline blade with bending stiffness variations shown in Figure 17. Significant reductions in objective function J are observed from r_{mid}=.60R to r_{mid}=.80R; the performance is somewhat less sensitive to flap location than in the baseline case in Fig. 17(c). In Fig. 21(b), the flap power required shows almost no variation due to torsional stiffness. In Figure 21(a), he flap deflections are reduced slightly with the torsionally softer configuration.

Taken as a whole, the flap performance results indicate that spanwise location of the flap is an important design parameter. However, since the controller algorithm adjusts the flap motions to compensate for

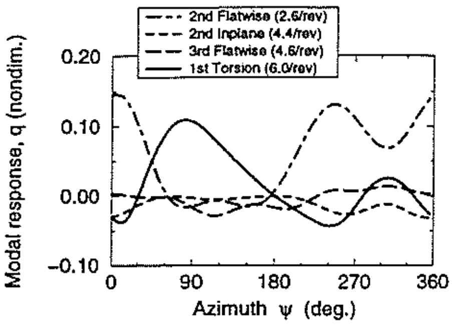

(a) Baseline (no flap input)

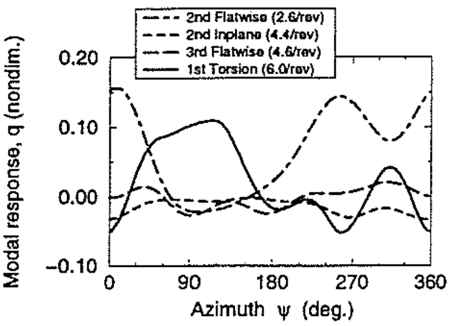

(b) Flap active, r_{mid}=.75R

Figure 19: Comparison of modal response of uncontrolled blade and blade with active flap at r_{mid}=.75R

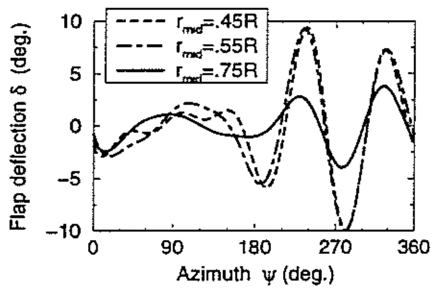

Figure 20: Trailing edge flap motions for baseline blade for three values of flap location r_{mid}

changes in the dynamic relationship between the flap and blade, the critical effect of spanwise placement is not, however, the ability of the flap to reduce vibratory hub loads. Rather, the importance of flap location is its effect on flap motions and power requirements.

Summary and Conclusions

The advantages of plain trailing edge flaps may now be realized with the development of compact, light weight smart structure actuators. An analytic model for helicopter main rotors with plain flaps has been developed, incorporating an advanced unsteady flap/airfoil aerodynamic model, full representation of the nonlinear inertial interactions of the flap and blade, free wake model, coupled trim procedure, and multicyclic algorithms.

A correlation study was performed using experimental data from a full scale bearingless main rotor. Fair to good agreement was seen in trim controls and blade inplane bending, and torsional moment. Poor correlation was observed for blade flatwise bending and fixed system N/rev hub loads. These difficulties were attributed to test stand dynamics.

A parametric design study examined flap location and variations in blade flatwise bending and torsional stiffness. The flaps were found to be very effective

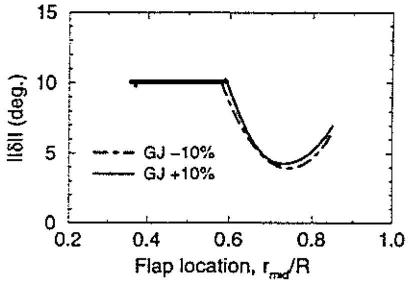

(a) Peak flap deflection

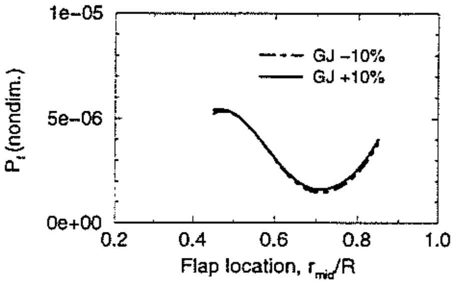

(b) Flap power required

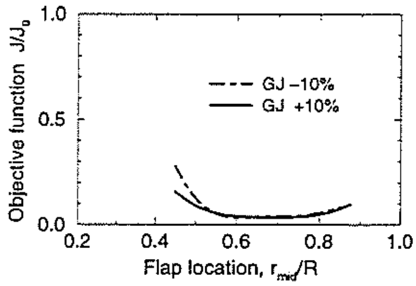

(c) Vibration objective function

Figure 21: Effect of trailing edge flap location (r_{mid}) on flap system performances for two values of blade torsional stiffness $\overline{GJ}$with wind tunnel trim at μ = 0.35.

in reducing N/rev hub loads, with reductions of up to 90% in vibration objective function. Proper spanwise placement of the flap is of critical importance in determining the flap motions and power requirements. Minimum actuation power and flap deflections occurred with the flap placed at 75% radius. However, the ability of the flap to reduce hub loads is not as sensitive to flap location since the control algorithm can compensate the placement effects to a limited extent by increasing the flap inputs.

The flap's most significant effect on modal response is to introduce a small higher harmonic component in the response of the first torsional mode.

Variations in blade flatwise bending and torsional stiffness of ±10% were found to have little effect on overall flap performance. In some cases, reducing these stiffnesses reduced the required flap inputs slightly. However, the hub loads reduction remained unchanged.

It is recommended that future research continue to examine the interaction between blade structural dynamic properties and trailing edge flap design. Larger stiffness variations than those considered in the present study need to be examined in order to identify clear trends. Other parameters such as blade mass distribution, center of gravity offset, and control system stiffness should be examined as well.

Acknowledgements

The authors gratefully acknowledge Dr. Friedrich Straub of McDonnell-Douglas Helicopter Systems for making available the design data and experimental results as well as providing valuable advice and assistance; Dr. Khanh Nguyen of NASA Ames Research Center for his assistance in preparing the correlation study; and Dr. Anita Tracy for her help in implementing the bearingless main rotor model.

References

[1] Raul Pateras Pescara. Screw propeller of helicopter flying machines. U.S. Patent 1,449,129, filed July 17, 1920, issued March 20, 1923.

[2] P. R. Payne. Higher harmonic rotor control. *Aircraft Engineering*, 30, 354, August 1958, pp 222–226.

[3] R. L. Spangler and S. R. Hall. Piezoelectric actuators for helicopter rotor control. In *Proceedings of the 31st AIAA Structures, Structural Dynamics, and Materials Conference*, Long Beach CA, April 1990. pp 1589–1599. Paper AIAA-90-1076-CP.

[4] C. Walz and I. Chopra. Design and testing of a helicopter rotor model with smart trailing edge flaps. In *Proceedings of the 35th Structures, Structural Dynamics and Materials Conference, Adaptive Structures Forum*, April 1994. AIAA-94-1767-CP.

[5] A. Bernhard and I. Chopra. Hover test of a smart flap actuated by a bending torsion coupled beam. In *Proceedings of the 37th AIAA/ASME/ASCE/AHS Structures, Structural Dynamics, and Materials Conference*, Salt Lake City, Utah, April 1996.

[6] Nikhil A. Koratkar and Inderjit Chopra. Testing and validation of a froude scaled helicopter rotor model with piezo-bimorph actuated trailing edge flaps. In *Proceedings of the SPIE Smart Structures and Materials Symposium*, San Diego, March 1997.

[7] F. K. Straub and Ahmed A. Hassan. Aeromechanical considerations in the design of a rotor with smart material actuated trailing edge flaps. In *Proceedings of the 52nd Annual National Forum of the American Helicopter Society*, Washington D.C., June 1996. pp 704–714.

[8] Mark V. Fulton and Robert A. Ormiston. Hover testing of a small-scale rotor with on-blade elevons. In *Proceedings of the 53rd Annual Forum of the American Helicopter Society*, Virginia Beach, Virginia, April-May 1997.

[9] A. Z. Lemnios and A. F. Smith. An analytical evaluation of the controllable twist rotor performance and dynamic behavior. USAMRDL TR 72-16, May 1972.

[10] J. L. McCloud III and Alfred L. Weisbrich. Wind tunnel test results of a full-scale multicyclic controllable twist rotor. In *Proceedings of the 34th Annual National Forum of the American Helicopter Society*, Washington, D.C., May 1978.

[11] T. A. Millott and P. P. Friedmann. The practical implementation of an actively controlled flap to reduce vibrations in helicopter rotors. In *Proceedings of the 49th Annual Forum of the American Helicopter Society*, St. Louis, May 1993. pp 1079–1092.

[12] T. A. Millott and P. P. Friedmann. Vibration reduction in hingeless rotors using an actively controlled trailing edge flap: Implementation and

time domain simulation. In *Proceedings of the 35th Structures, Structural Dynamics and Materials Conference, Adaptive Structures Forum*, April 1994. AIAA-94-1306-CP.

[13] W. Johnson. Self-tuning regulators for multicyclic control of helicopter vibration. NASA Technical Paper 1996, March 1982.

[14] I. I. Sikorsky. Direct lift aircraft. U. S. Patent 1,994,488, filed June 27, 1931, issued March 19, 1935.

[15] D. Dinkler and F. Doengi. Robust vibration control of rotor blades in forward flight. In *Proceedings of the CEAS International Forum on Aeroelasticity and Structural Dynamics*, Manchester, UK, June 1995.

[16] F. K. Straub and L. H. Robinson. Dynamics of a rotor with nonharmonic control. In *Proceedings of the 49th Annual Forum of the American Helicopter Society*, St. Louis, Missouri, May 1993. pp 1067–1078.

[17] S. Dawson and F. Straub. Design, validation, and test of a model rotor with tip mounted active flaps. In *Proceedings of the 50th Annual Forum of the American Helicopter Society*, Washington DC, May 1994.

[18] F. K. Straub. Active flap control for vibration reduction and performance improvement. In *Proceedings of the 51st Annual Forum of the American Helicopter Society*, Fort Worth, Texas, May 1995.

[19] J. H. Milgram and I. Chopra. Helicopter vibration reduction with trailing edge flaps. In *Proceedings of the American Helicopter Society Northeast Region Aeromechanics Specialists Meeting*, Stratford, CT, October 1995.

[20] J. H. Milgram, I. Chopra, and F. Straub. A comprehensive rotorcraft aeroelastic analysis with trailing edge flap model: Validation with experimental data. In *Proceedings of the 52nd Annual Forum of the American Helicopter Society*, June 1996.

[21] Judah H. Milgram. *A Comprehensive Aeroelastic Analysis of Helicopter Main Rotors with Trailing Edge Flaps for Vibration Reduction.* PhD thesis, University of Maryland, College Park, Maryland, January 1997.

[22] G. Bir, I. Chopra, et al. University of Maryland Advanced Rotor Code (UMARC) Theory Manual. Technical Report UM-AERO 94-18, Center for Rotorcraft Education and Research, University of Maryland, College Park, Maryland, July 1994.

[23] Anita L. Tracy and I. Chopra. Aeroelastic analysis of a composite bearingless rotor in forward flight using an improved warping model. *Journal of the American Helicopter Society*, 40, 3, July 1995, pp 35–91.

[24] N. Hariharan and J. G. Leishman. Unsteady aerodynamics of a flapped airfoil in subsonic flow by indicial concepts. In *Proceedings of the 36th AIAA/ASME/ASCE/AHS/ASC Structures, Structural Dynamics, and Materials Conference*, New Orleans, LA, April 1995.

[25] A. Bagai and J. G. Leishman. Rotor free-wake modeling using a pseudo-implicit technique - including comparisons with experimental data. *Journal of the American Helicopter Society*, 40, 3, July 1995.

[26] John Shaw et al. Higher harmonic control: Wind tunnel demonstration of fully effective vibratory hub force suppression. *Journal of the American Helicopter Society*, 34, 1, January 1989, pp 14–25.

[27] M. J. McNulty. A full-scale test of the McDonnell Douglas Advanced Bearingless Rotor in the NASA Ames 40- b 80-ft wind tunnel. In *Proceedings of the 49th Annual Forum of the American Helicopter Society*, St. Louis, May 1993. pp 1535–1544.

[28] Khanh Nguyen. Aeroelastic stability of the McDonnell Douglas Advanced Bearingless Rotor. In *Proceedings of the 49th Annual Forum of the American Helicopter Society*, St. Louis, May 1993. pp 1283–1290.

[29] Khanh Nguyen. Computation of loads on the McDonnell Douglas Advanced Bearingless Rotor. In *Proceedings of the 50th Annual Forum of the American Helicopter Society*, Washington, DC, May 1994. pp 337–346.